BEILSTEIN JOURNAL OF NANOTECHNOLOGY

Supporting Information

for

Kinetically controlled boron carbide composite sub-micrometer particle formation pathways during continuous-flow laser melting in liquids with high-power lasers

Nico G. Koch, Christoph Rehbock, Naoto Koshizaki and Stephan Barcikowski

Beilstein J. Nanotechnol. **2026,** *17,* 1582–1595. doi:10.3762/bjnano.17.108

Additional experimental data

License and Terms: This is a supporting information file under the terms of the Creative Commons Attribution License (https://creativecommons.org/licenses/by/4.0). Please note that the reuse, redistribution and reproduction in particular requires that the author(s) and source are credited and that individual graphics may be subject to special legal provisions.
The license is subject to the *Beilstein Journal of Nanotechnology* terms and conditions: (https://www.beilstein-journals.org/bjnano/terms)

Section S1: Laser Setup and Parameter Calculation

To ensure homogeneous irradiation while minimizing undesirable phenomena such as back mixing (which otherwise happens in batch reactors) and laser beam refraction at the air–liquid interface, a flat jet configuration is employed. This flat jet arrangement facilitates a more uniform exposure of the liquid medium by the laser pulse, thereby enhancing process control and reproducibility. The setup is shown below.

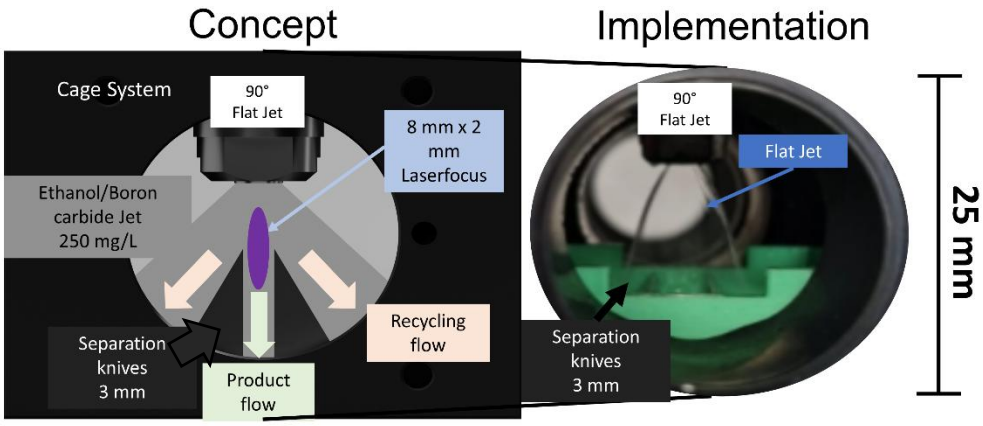


Figure S1: Schematic setup for continuous-flow laser melting in liquid using a flat jet with recycling of the unirradiated fraction to minimize loss of educt particles (left image). Implementation of the flat jet in the setup (right image).

Table S1: Setup parameters.

Laser parameters	Flat jet parameters
• wavelength: 343 nm • pulse duration: 18 ± 3 ns • pulse energy: 0.6 mJ • repetition rate: 10 kHz • beam area: 0.12 cm^2 (1/e^2 criterion) • fluence = $\frac{\textbf{Pulse energy}}{\textbf{Beam area}}$	• flow rate: 3.4 $L \cdot h^{-1}$ • flat jet depth: 35 µm • horizontal diameter of the laser beam: 2 mm (1/e^2 criterion) • vertical diameter of the laser beam: 8 mm (1/e^2 criterion) • linear speed: 4.8 ± 1.1 $m \cdot s^{-1}$

UV–vis measurement to determine the flat jet thickness

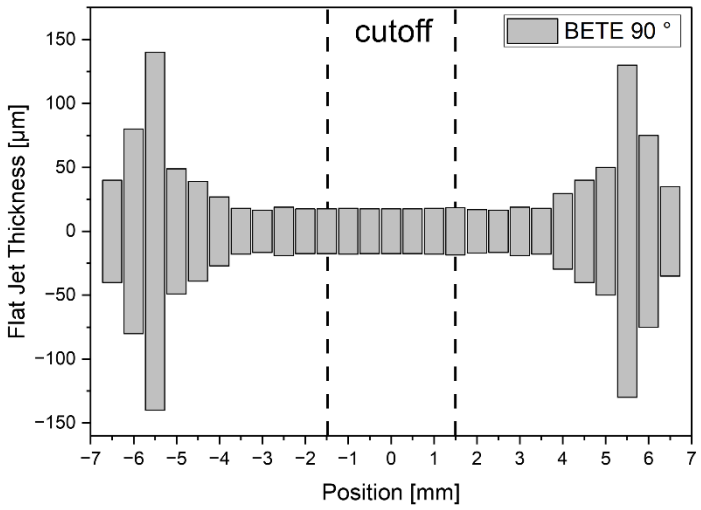


Figure S2: The thickness of the flat jet (BETE 90° flat jet nozzle) was measured using the Beer–Lambert's law, as described by Zerebecki et al. [1], with a homogeneous thickness of 35 ± 2 µm in the marked area (2 mm laser diameter, centered at position 0); the cut-off lines mark the separation knive position.

Flow conditions

According to Friedenauer et al. [2], the Reynolds number in flat jet systems can be calculated as follows:

$$\mathrm{Re_{FJ}} = \frac{\rho v d_{\mathrm{hydr}}}{\eta},$$

where $\mathrm{Re_{FJ}}$ is the Reynolds number of the flat jet system; ρ is the fluid density; *v* is the flow velocity; d_{hydr} is the diameter; and η is the dynamic viscosity of the fluid. The diameter, is determined by:

$$d_{\mathrm{hydr}} = \frac{4A}{U},$$

where A represents the cross-sectional area and *U* is the wetted perimeter of the jet geometry.

Section S2: Analysis Feedstock and LML Particles

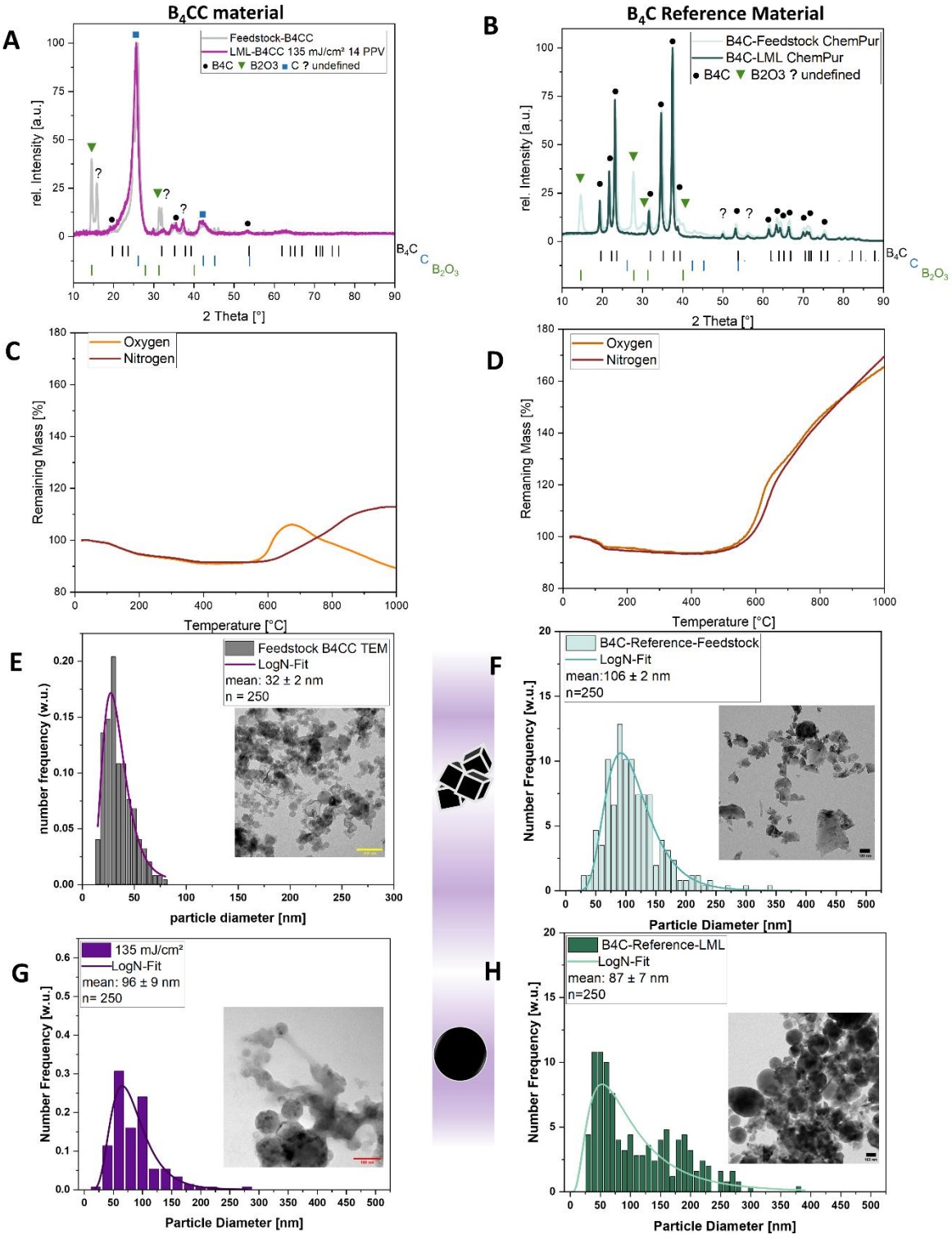


Figure S3: (A) Smoothed XRD patterns of the feedstock boron carbide composite (B_4CC), the LML B_4CC product, and the corresponding ICSD reference. (B) XRD patterns of the feedstock boron carbide reference from ChemPur, the LML B_4C product, and the corresponding ICSD reference. (C, D) TGA curves of the feedstock B_4CC and the reference B_4C in oxygen and nitrogen atmospheres at 100 mL·min^{-1} gas flow and a heating rate of 25 °C·min^{-1}. (E, F) TEM images of the feedstock B_4CC and B_4C. (G, H) Corresponding TEM images after LML processing at 135 mJ·cm^{-2}.

To resolve the compositional ambiguity of the boron carbide feedstock, we first analyzed the X-ray diffraction patterns of the B_4CC sample and compared them with those of pristine B_4C (see Figure S3A,B). Analysis of the crystallite size of the pristine B_4C, evaluated at $2\theta = 37.64°$, yields a crystallite size of approximately 13 nm. In contrast, the diffraction pattern of the B_4CC sample lacks sufficient peak definition to permit reliable determination of the crystallite size, indicating either a reduced degree of crystallinity or the presence of structurally disordered phases. Notably, the crystallite size of the pristine material is significantly smaller than the observed particle diameter for the submicron spheres, indicating that these particles are polycrystalline in nature. This suggests that the spheres consist of multiple smaller crystalline domains derived from the original feedstock particles, which melted together during processing. The lattice parameters obtained for the pristine B_4C are in good agreement with the reference values reported in the ICDD database, thereby confirming the phase purity and correct structural assignment of the material. In contrast, the diffraction pattern of the B_4CC sample cannot be clearly matched to known patterns in the database, thereby confirming the presence of a composite material. The diffractogram is dominated by a pronounced broad peak between 20° and 30°, which could be loosely associated with graphitic carbon. It may also indicate the presence of amorphous boron or carbon, while sharp peaks indicative of crystalline boron oxide and graphite phases are found, which is consistent with previous reports [3]. However, the absence or very weak expression of characteristic B_4C peaks indicates that only minor fractions of crystalline boron carbide are present in the B_4CC sample. Following laser melting in a liquid environment, both the B_4CC and the B_4C reference samples exhibit a similar evolution in their diffraction patterns. Reflections associated with boron oxide, which were initially present in the feedstock, are no longer observed after processing. This

indicates that the laser melting process effectively removes or transforms boron oxide species.

We then examined the thermal response by thermogravimetric analysis under oxidizing (O_2) and inert (N_2) atmospheres to further understand the nature of the composite. In parallel, we analyzed a second boron carbide powder obtained from an alternative supplier (ChemPur) as a reference feedstock material of higher purity, as shown by XRD (see Figure S3B). Thermogravimetric analysis in the presence of oxygen (shown in Figure S3C,D) reveals a comparatively low mass increase of 20.9% for the B_4CC feedstock NPs from Nanografi. Assuming that only B_4C undergoes oxidation and adopting the reaction stoichiometry reported by Chaparro-Pérez et al.[4], complete conversion would correspond to a theoretical mass gain of 101.4%. The experimentally observed increase, therefore, indicates that only approximately 20.6% of the sample consists of stoichiometric B_4C. Based on the combined TGA and XRD results, the commercial feedstock (B_4C) can be identified as a heterogeneous mixture containing ~21 wt % pure B_4C, alongside a predominant fraction of graphitic or amorphous carbon and pre-existing boron oxide. This is further corroborated by XPS analysis of the feedstock before LML, which yields a carbide content of ~21 atom % (Figure S4), in direct alignment with the TGA quantification (Figure S3A). Thermogravimetric analysis under a nitrogen atmosphere confirmed that the remaining non-constituents are largely inert during thermal ramp-up and do not contribute to measurable mass changes before laser treatment. Such strong deviations from ideal stoichiometry directly impact thermophysical parameters relevant for numerical modelling, including heat capacity, thermal conductivity, and optical absorption. This means that simulated absolute thresholds may show systematic offsets from the experimental system. These compositional insights are also critical for interpreting the state of the material after irradiation. While the initial B_2O_3 phase is effectively removed

or transformed during laser processing in liquids (as confirmed by the disappearance of its XRD reflections and further supported by XPS analysis before and after LML, which clearly indicates a reduction in surface oxidation in Figure S4C,D), the high carbon content presents a distinct physical scenario. However, we should still add that boron oxide can be dissolved in ethanol under certain conditions. Figure S3A shows a clear tail extending from the graphite peak towards the B_4C reflections, indicating an atomically mixed state of boron within the graphitic domain. As can be seen from the phase diagram, when these boron–carbon composite mixtures co-exist with graphite, they can undergo melt-quenching processes that enable the formation of dense, spherical particles. Pure graphitic carbon, by contrast, does not undergo conventional liquid-phase melting under typical ambient processing pressures, but rather sublimes at extreme temperatures or remains solid. Consequently, dense, spherical droplets cannot be formed directly from the carbon-rich matrix via classical liquid coalescence. Instead, SMS formation is predominantly driven by the melting, coalescence, and resolidification of the high-melting fraction, for which the required melting fluence matches the thresholds determined experimentally and numerically. However, given that XRD analysis confirms the continued presence of carbon even after laser irradiation, the resulting B_4C SMSs cannot be considered phase-pure spheres. Instead, they are composite structures comprising melted and resolidified domains alongside non-melted graphitic or amorphous carbon fractions and residual transient species. To further substantiate this assignment, comparative experiments were conducted using a nominally pure B_4C reference material (ChemPur) for LML. LML of both feedstock materials at 135 $mJ \cdot cm^{-2}$ (Figure S3E–H) yields B_4C SMSs with comparable morphologies and size distributions, which indicates that both materials possess comparable melting behavior. In this work, we primarily used the B_4CC feedstock materials as their narrower size distribution and smaller initial particle size

distributions were more suitable to mechanistically elucidate and differentiate isochoric melting and melting-fusion-based particle formation pathways. This differentiation is essential to accurately map the kinetics of phase transformations during laser irradiation. If B_4C was used exclusively, its broad size distribution would make it more difficult to differentiate between changes in particle size caused by isochoric remelting of individual particles and aggregation and fusion melting of multiple adjacent particles. Therefore, the B_4CC nanoparticles with a narrower size distribution were selected to isolate particle size as a variable. Thereby, size shifts can be unequivocally attributed to specific physical phenomena. This enabled us to clearly decipher the underlying physical mechanisms without the confounding effects of a highly dispersed initial particle size distribution.

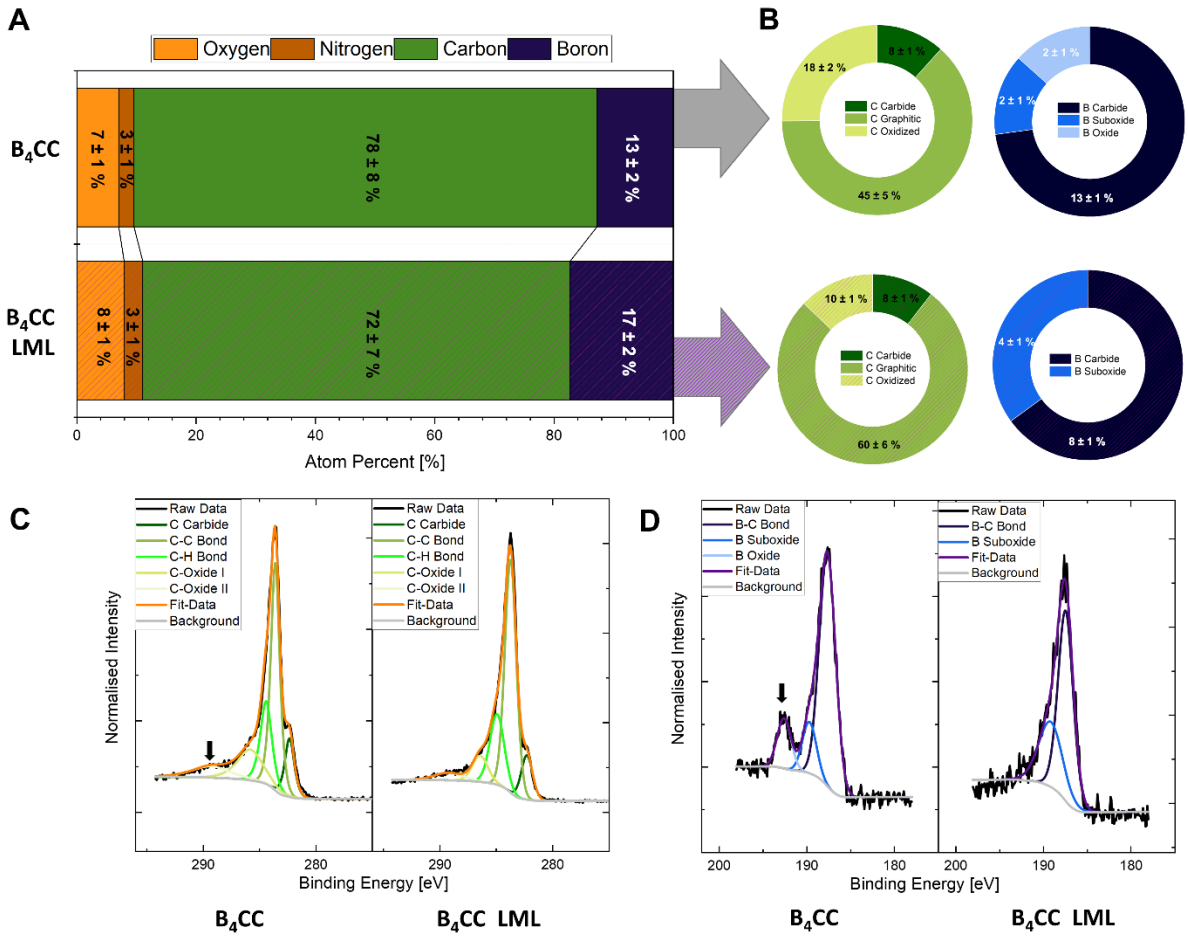


Figure S4: (A) Elemental atomic concentrations of oxygen (orange), nitrogen (brown), carbon (green), and boron (dark blue), as determined by X-ray photoelectron spectroscopy, for pristine B_4CC feedstock (top) and processed colloid after LML treatment (B_4CC LML, bottom). (B) Quantitative speciation of carbon (green donut charts, left) and boron (blue donut charts, right), showing the chemical binding states. (C) XPS spectra of B_4CC (left) and B_4CC LML (right), showing raw data, background fitting, and deconvolution of the carbon peak. (D) XPS spectra of B_4CC (left) and B_4CC LML (right), showing raw data, background fitting, and deconvolution of the boron peak. Black arrows highlight the reduction of surface-oxidized carbon components.

Section S3: Feedstock Nanoparticle Size Characterization

As described in the main manuscript, the feedstock characterization is essential to ensure that our LML results are due solely to laser–matter interaction and not to preexisting size fractions in the starting material.

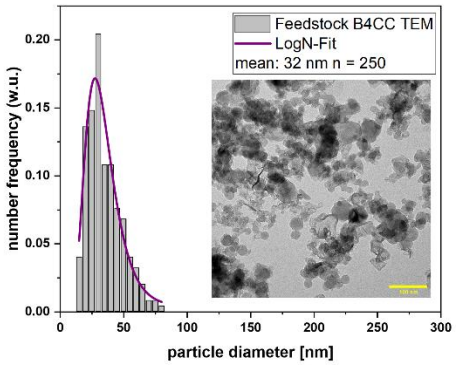


Figure S5: TEM results of the feedstock after the purification described in the Experimental section.

Section S4: HME Model Calculation Script and Fluence Series

Calculation of the LML and LFL regions in the size–fluence diagram

The implemented calculations (parameters are provided in Tables S2–S5) were derived from the methodology established by Sakaki et al. [6] and subsequently adapted for execution in Matlab. This adaptation was complemented by several methodological extensions, notably the incorporation of heat capacity as a temperature-dependent variable, the dynamic Nusselt number, and the explicit consideration of Kapitza resistance in the thermal transport modeling. Recent simulations by Zhigilei et al. [7] demonstrated (for a gold surface and ultrashort pulse durations) that supercritical solvent layers at the nanoparticle–liquid interface are curvature-dependent and can alter the thermal conductance by up to an order of magnitude, which could shift the predicted fluence required for melting to higher values. Moreover, Zhigilei et al. [7] showed that the heat transfer (under identical conditions) depends on the curvature of the solid surface, which means that HME simulations of the LML (and LFL) would need to consider the particle size dependence of the heat transfer coefficient. For gold and sizes from bulk to 7 nm, the coefficient changed by 20–30%, not considered in our calculations below (as such simulation results are neither available for boron carbide nor for nanosecond pulses). The model presented

here has only been experimentally validated for B_4CC particles (see Figure S5). Therefore, it is important to exercise caution when applying this theory to other material systems as its validity and predictive accuracy for these systems has not yet been established through experimental testing.

Table S2: Material parameters and thermodynamic constants.

Parameter	Value	Unit	Meaning
ρ_p	2520	$kg \cdot m^{-3}$	particle density [8]
T_m	2623.15	K	melting temperature [8]
T_{eva}	3776	K	approximate evaporation temperature [9]
ΔH_m	$1.9674 \cdot 10^6$	$J \cdot kg^{-1}$	approximate melting enthalpy [10]
$H(T_m) - H(T_0)$	$4.82108 \cdot 10^6$	$J \cdot kg^{-1}$	approximate heat to melting [10]
N	3.1041	—	refractive index real part [11]
K	0.9112755	—	refractive index imaginary part [11]
Λ	343	nm	laser wavelength
$T_{spinodal}$	351.5	K	spinodal temperature (NIST)
Γ	1.0	$N \cdot m^{-1}$	surface tension (NIST)
R	8.314	$J \cdot mol^{-1} \cdot K^{-1}$	gas constant
$\alpha_{superheat}$	1.7	—	superheat factor
P_1	101325	Pa	ambient pressure

Table S3: Thermal properties of ethanol (interpolation points).

Thermal Conductivity - Liquid Phase		
Temperature (K)	κ_{liquid} ($W \cdot m^{-1} \cdot K^{-1}$)	Meaning
293	0.171	liquid thermal conductivity (NIST)
351.5	0.150	liquid thermal conductivity (NIST)
Thermal Conductivity - Vapor Phase		
Temperature (K)	κ_{vapor} ($W \cdot m^{-1} \cdot K^{-1}$)	Meaning
351.5	0.023	vapor thermal conductivity (NIST)
600	0.027	vapor thermal conductivity (NIST)

Table S4: Convection and flow parameters (Nusselt correlation)

Parameter	Value	Unit	Meaning
G	9.81	$m \cdot s^{-2}$	gravitational acceleration
v (kinematic viscosity)	$1.52 \cdot 10^{-6}$	$m^2 \cdot s^{-1}$	ethanol kinematic viscosity[12]
α (thermal diffusivity)	7.3×10^{-8}	$m^2 \cdot s^{-1}$	ethanol thermal diffusivity[12]

Nusselt correlation: $Nu = 2 + 0.6 \cdot Ra^{(1/4) \cdot Pr} 0.074$

Table S5: Laser and simulation parameters.

Parameter	Value	Unit	Meaning
τ_{pulse} (FWHM)	14	ns	pulse duration full width half maximum (Trumpf)
Δt	0.1	ns	time step
t_0	7	ns	approximately pulse center time

```
clear; clc;
d_vector = linspace(10e-9, 500e-9, 100);
fluence_vector = linspace(10, 500, 100)*1e-3*1e4;
rho_p = 2520;
T_m = 2623.15;
T_eva = 3776;
delta_Hm = 1.9674e6;
H_Tm_H_T0 = 4.82108e6;
n = 3.1041; k = 0.91127[11]; lambda = 343e-9;
T_0 = 298; T_spinodal = 351.5;
k_ethanol_liq = @(T) interp1([293, 351.5], [0.171, 0.150], min(T, 351.5),
'linear', 'extrap');
k_ethanol_vap = @(T) interp1([351.5, 600], [0.023, 0.027], max(T, 351.5),
'linear', 'extrap');
c_s_T = @(T) interp1([300, T_m], [400, 600], T, 'linear', 'extrap');
c_l_T = @(T) interp1([T_m, 4000], [600, 650], T, 'linear', 'extrap');
gamma = 1.0;
R_gas = 8.314;
delta_H_vap = 2.5e6;
h_interface = 6e7;
alpha_superheat =1.7;
max_temperature = zeros(length(fluence_vector), length(d_vector));
for f_idx = 1:length(fluence_vector)
    fluence = fluence_vector(f_idx);
    pulse_width = 14e-9;
    t_max = 3 * pulse_width;
    dt = 0.1e-9;
    t = 0:dt:t_max;
    t0 = 7e-9;
    J_peak = fluence / (sqrt(pi/(4*log(2))) * pulse_width);
    J_t = J_peak * exp(-4*log(2) * ((t - t0).^2) / pulse_width^2);
    for d_idx = 1:length(d_vector)
        d = d_vector(d_idx);
        A_abs = pi * (d/2)^2;
        A_loss = pi * d^2;
        V_p = (pi/6) * d^3;
        m_p = rho_p * V_p;
        Q_abs = getQabs_Mie(d, n, k, lambda);
        T = zeros(size(t));
        T(1) = T_0;
        E = 0;
        fragmented = false;
        r = d/2;
        delta_P_Laplace = 2 * gamma / r;
        P1 = 101325;
        P2 = P1 + delta_P_Laplace;
        T_frag_Laplace = 1/((1/T_eva) - (R_gas/delta_H_vap)*log(P2/P1));
        T_frag = T_frag_Laplace * alpha_superheat;
        for i = 2:length(t)
            dE_abs = Q_abs * A_abs * J_t(i) * dt;
            Nu = getNu(d, T(i-1), T_0);
            if T(i-1) < T_spinodal
                k_thermal = k_ethanol_liq(T(i-1));
            else
                k_thermal = k_ethanol_vap(T(i-1));
            end
            h_fluid = Nu * k_thermal / d;
            h_total = 1 / (1/h_interface + 1/h_fluid);
            dQ_loss = h_total * A_loss * (T(i-1) - T_0) * dt;
            dE_netto = dE_abs - dQ_loss;
            E = E + dE_netto;
```

```
            if T(i-1) >= T_frag
                fragmented = true;
            end
            if fragmented
                T(i) = T_frag;
            else
                if E < m_p * H_Tm_H_T0
                    c_eff = c_s_T(T(i-1));
                    T(i) = T_0 + E / (m_p * c_eff);
                elseif E < m_p * (H_Tm_H_T0 + delta_Hm)
                    T(i) = T_m;
                else
                    c_eff = c_l_T(T(i-1));
                    E_fl = E - m_p * (H_Tm_H_T0 + delta_Hm);
                    T(i) = T_m + E_fl / (m_p * c_eff);
                end
            end
        end
        max_temperature(f_idx, d_idx) = max(T);
    end
end
function Qabs = getQabs_Mie(d, n, k, lambda)
    m = n + 1i * k;
    x = pi * d / lambda;
    result = mie(m, x);
    Qabs = result(6);[13]
end
function Nu = getNu(d, T, T_sur)
    g = 9.81;
    beta = 1 / T_sur;
    nu = 1.52e-6;
    alpha = 7.3e-8;
    Pr = nu / alpha;
    Ra = g * beta * abs(T - T_sur) * d^3 / (nu * alpha);
    if Ra < 1
        Nu = 2;
    else
        Nu = 2 + 0.6 * Ra^(1/4) * Pr^0.074;
    end
end
```

Fluence series

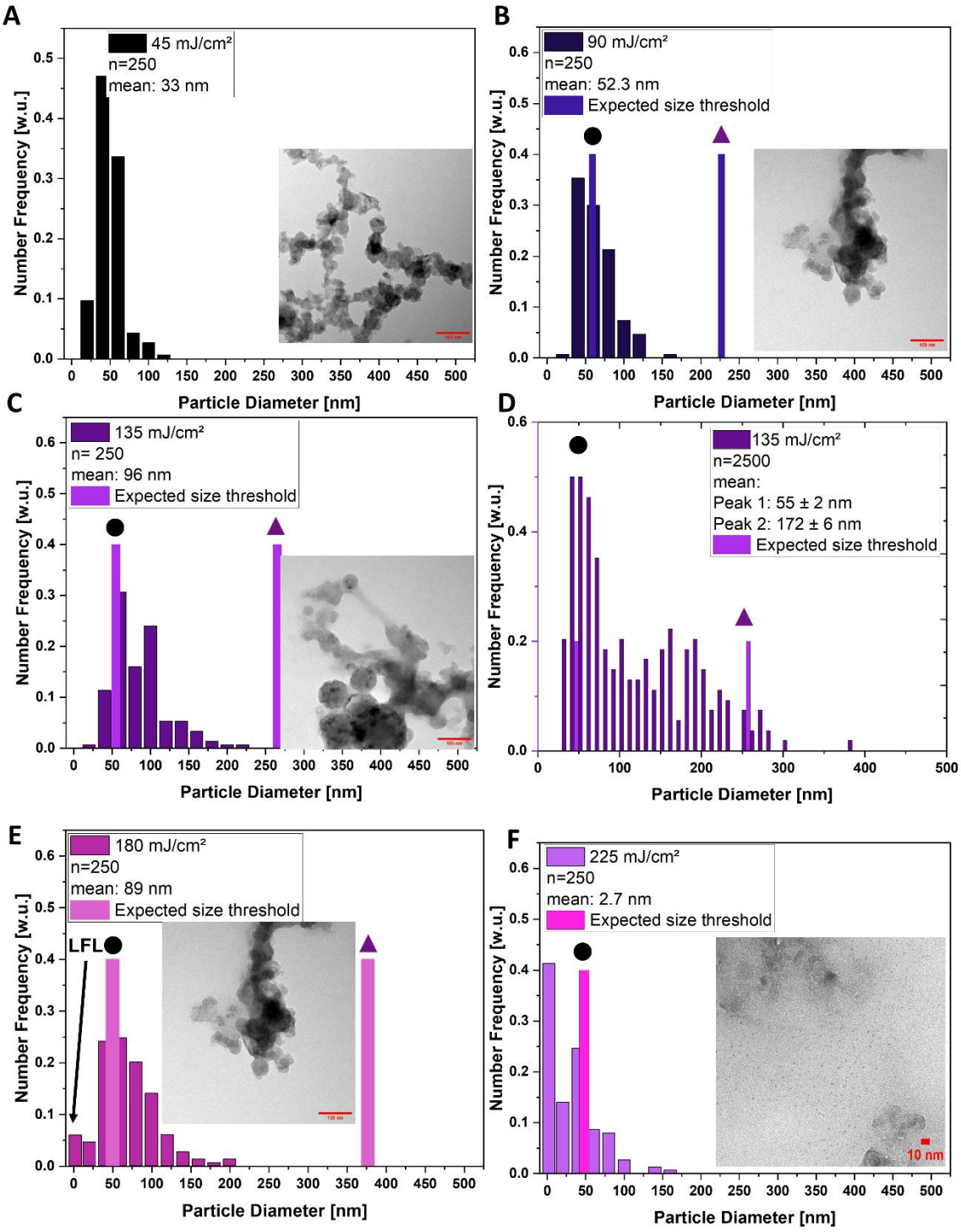


Figure S6: TEM size histograms (n = 250) of the fluence series (A) 45 mJ·cm^{-2}, (B) 90 mJ·cm^{-2}, (C) 135 mJ·cm^{-2}, (D) 135 mJ·cm^{-2} with n = 2500 to see the bimodal size distribution, (E) 180 mJ·cm^{-2}, and (F) 225 mJ·cm^{-2} with marked expected size threshold (from the model calculation in Section S4).

Ultrasmall nanoparticles

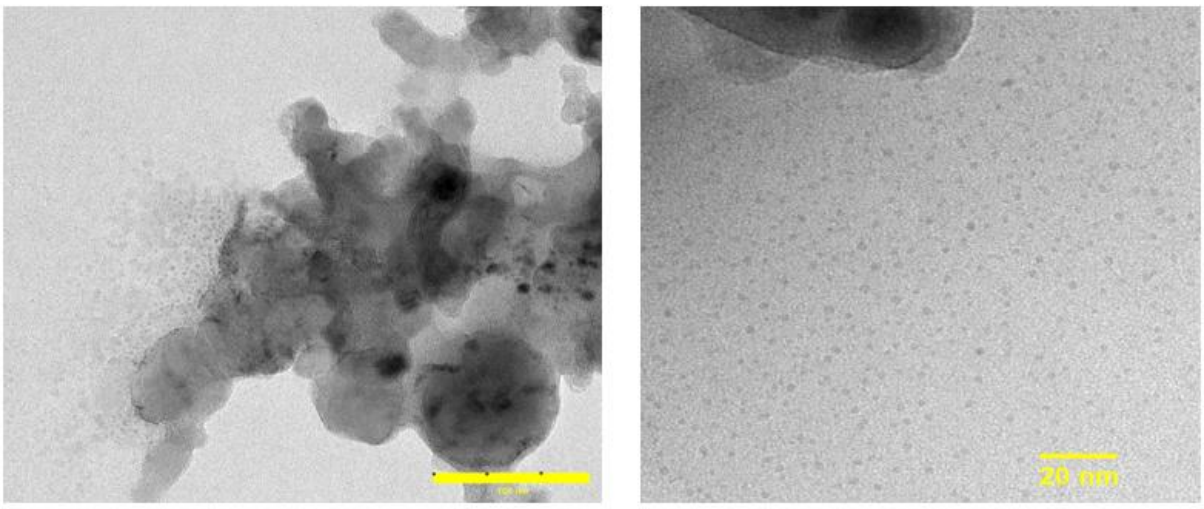


Figure S7: TEM images of the 180 mJ·cm^{-2} (left) and 225 mJ·cm^{-2} (right) samples proving the LFL products of numerous ultrasmall NPs.

SEM

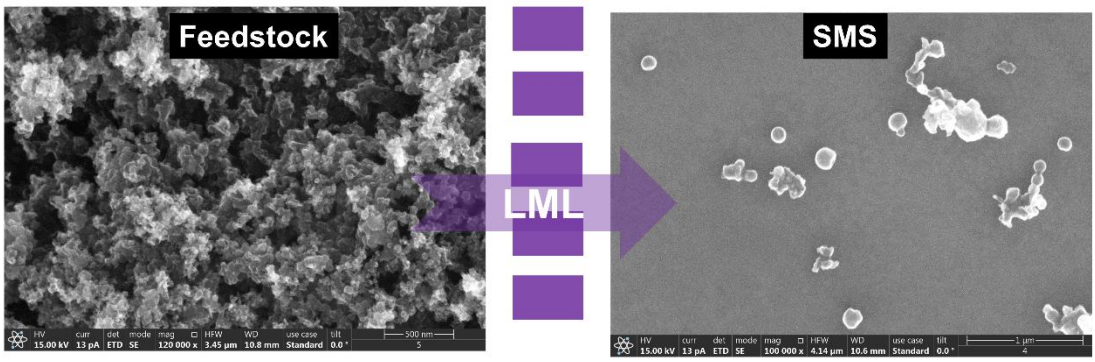


Figure S8: SEM images of the untreated feedstock and LML-produced SMS at 135 mJ·cm^{-2}.

Section S5: PPV Series

Number of laser pulses per unit volume (PPV):

$$\mathrm{PPV} = \frac{\text{vertical diameter of the laser beam}}{\text{linear speed of the liquid jet}} \cdot \text{repetition rate}$$

Table S6: Divider settings for the PPV Series.

Rounded PPV	Inter-pulse delay time [ms]	Divider value	Output repetition rate [kHz]
1	1.40	14	0.71
2	0.80	8	1.25
3	0.50	5	2.00
4	0.40	4	2.50
8	0.20	2	5.00
16	0.10	1	10.0

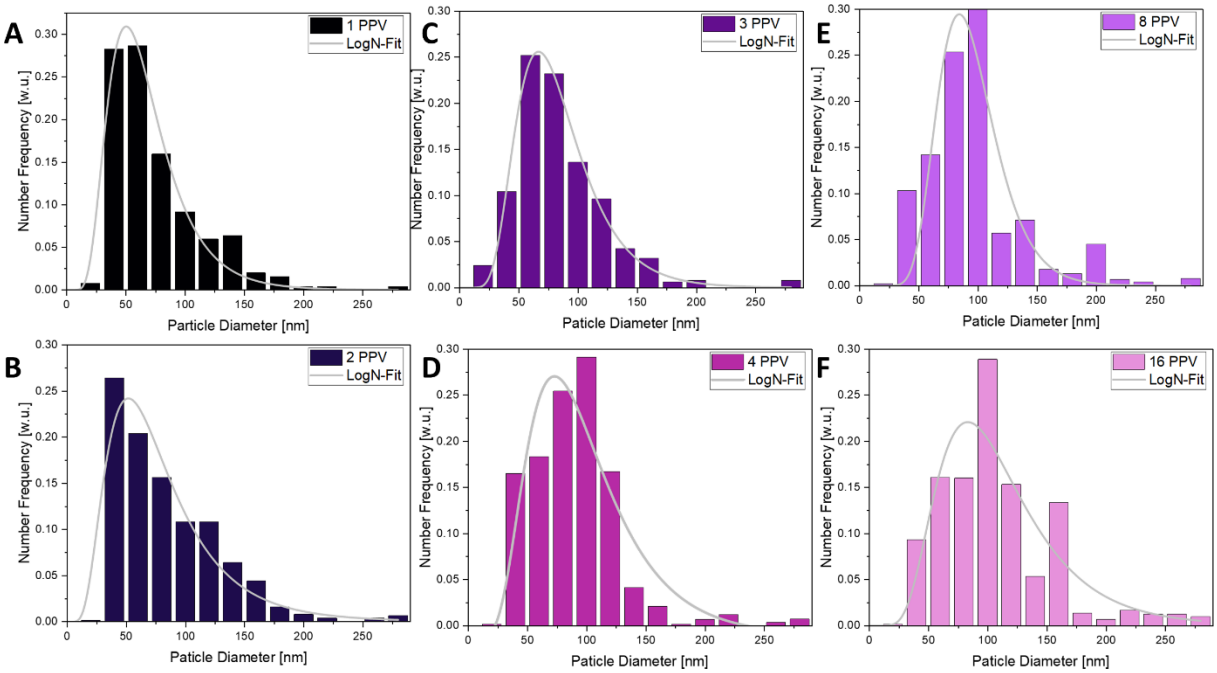


Figure S9: TEM-derived particle diameter histograms (n = 250) of the PPV series (A) 1 PPV, (B) 2 PPV, (C) 3 PPV, (D) 4 PPV, (E) 8 PPV, and (F) 16 PPV with LogN fits.

Section S6: Productivity and Scale-Up

TEM imaging combined with dispersion analysis indicates that particles with diameters of 80 nm or larger undergo complete conversion to SMSs during LML. SMS formation productivity is thus quantified by integrating the optically illuminated fraction, two thirds of the total cross-sectional area, with a 50% mass conversion rate from the particle size distribution (Figure 2 in the main manuscript). This approach captures the effective reactor volume for LML, yielding precise mass productivity under defined conditions, using a particle concentration of 250 $mg \cdot L^{-1}$, volume flow of 1.2 $L \cdot h^{-1}$, and irradiation across the channel diameter. For optimized control, a maximum laser power of 400 W was applied to achieve an illumination profile of 18 mm length and 2 mm width, maintaining laser fluence at 135 $mJ \cdot cm^{-2}$, the regime yielding the highest SMS formation productivity without inducing LFL. This full cross-section illumination eliminates the prior geometric correction factor of 0.66. Consequently, throughput (L/h) per irradiated millimeter rises substantially, which scales the product flow rate to 7.2 L/h. With constant initial particle concentration (250 $mg \cdot L^{-1}$), constant PPV, and constant linear flow rate, the expanded laser-illuminated width at fixed fluence proportionally increases the volume flow rate. These adjustments could yield an SMS formation productivity of 900 $mg \cdot h^{-1}$.

$$P_{\mathrm{SMS}} = \eta_{\mathrm{mass}} \cdot f_{\mathrm{illum}} \cdot c_0 \cdot \dot{V} \qquad \text{(S1)}$$

Table S7: Description of the formula symbols.

Symbol	Meaning
P_{SMS}	SMS formation productivity
η_{mass}	mass conversion rate
f_{illum}	illumination factor
c_0	particle concentration
$\dot{V}$	volumetric flow rate

$$\text{productivity}\,(\text{Current flat jet}) = 0.5 \cdot 0.66 \cdot 250\,\frac{\text{mg}}{\text{L}} \cdot 1.2\,\frac{\text{L}}{\text{h}} = 99\,\frac{\text{mg}}{\text{h}} \quad \text{(S2)}$$

productivity (fully illuminated flat jet) = 0.5 · 250 mg/L ·7.2 L/h = 900 mg/h

References

1. Zerebecki, S.; Reichenberger, S.; Barcikowski, S. *J. Phys. Chem. A* **2020,** *124,* 11125–11132. doi:10.1021/acs.jpca.0c08787
2. Friedenauer, T.; Spellauge, M.; Sommereyns, A.; Labenski, V.; Esatbeyoglu, T.; Rehbock, C.; Huber, H. P.; Barcikowski, S. *Beilstein J. Nanotechnol.* **2025,** *16,* 711–727. doi:10.3762/bjnano.16.55
3. Tran, B. H.; Tieu, K.; Wan, S.; Zhu, H.; Cui, S.; Wang, L. *RSC Adv.* **2018,** *8,* 28847–28860. doi:10.1039/C8RA04658A
4. Chaparro-Pérez, K. D.; Lartundo-Rojas, L.; Olivares-Luna, M.; Rosales-Lopez, J. L.; Delgado-Brito, A. M.; Palomar-Pardavé, M.; Campos-Silva, I. *Surf. Interfaces* **2025,** *76,* 107760. doi:10.1016/j.surfin.2025.107760
5. Ishak, R.; Picard, D.; Laroche, G.; Ziegler, D. P.; Alamdari, H. *Metals (Basel, Switz.)* **2017,** *7,* 79. doi:10.3390/met7030079

6. Sakaki, S.; Ikenoue, H.; Tsuji, T.; Ishikawa, Y.; Koshizaki, N. *ChemPhysChem* **2017,** *18,* 1101–1107. doi:10.1002/cphc.201601175
7. Arefev, M. I.; Valavanis, A. S.; Zhigilei, L. V. *J. Phys. Chem. C* **2026,** *130,* 1042–1066. doi:10.1021/acs.jpcc.5c06989
8. Boron Carbide (B4C) Nanopowder/Nanoparticles https://shop.nanografi.com/nanoparticles/boron-carbide-b4c-nanopowder-nanoparticles-purity-99-5-size-40-60-nm-hexagonal/ (accessed Nov 17, 2025)
9. *CRC Handbook of Chemistry and Physics: A Ready-Reference Book of Chemical and Physical Data*, 97th ed.; Haynes, W. M., Ed.; CRC Press: Boca Raton London New York, 2017.
10. Properties: Boron Carbide (B4C) - Properties and Information about Boron Carbide https://www.azom.com/properties.aspx?ArticleID=75 (accessed Dec 18, 2025)
11. Larruquert, J. I.; Pérez-Marín, A. P.; García-Cortés, S.; Rodríguez-de Marcos, L.; Aznárez, J. A.; Méndez, J. A. *J. Opt. Soc. Am. A* **2012,** *29,* 117. doi:10.1364/JOSAA.29.000117
12. Poling, B. E.; Prausnitz, J. M.; O'Connell, J. P. *Properties of Gases and Liquids, Fifth Edition*, Fifth edition.; McGraw-Hill's AccessEngineering; McGraw-Hill Education: New York, N.Y, 2020